



Cite this: *RSC Adv.*, 2018, 8, 19600

Investigation of crystal structure, microstructure and low temperature magnetic behavior of Ce⁴⁺ and Zn²⁺ co-doped barium hexaferrites (BaFe₁₂O₁₉)

Khagesh Tanwar, * Deepankar Sri Gyan, Prashant Gupta, Shukdev Pandey, OmParkash and Devendra Kumar

Ce⁴⁺ and Zn²⁺ co-doped barium hexaferrites (BFO) have been synthesized *via* a citrate-nitrate autocombustion route. Phase purity has been confirmed by high resolution (HR) powder X-ray diffraction analysis. Rietveld refinement on HR-XRD data has been carried out to reveal the crystal structure, bond angles and bond lengths. High-resolution scanning electron microscope (HR-SEM) has been used to study the effect of Ce⁴⁺ and Zn²⁺ on microstructure. Magnetic behavior of co-doped barium hexaferrites in the low temperature regime, 2–300 K has been studied. Further, it has been explained on the basis of superexchange interactions and formation of Bloch walls due to the presence of imperfections in the doped samples. It has been found that BFO changes hard to soft magnetic behavior when the temperature is decreased from 300 K to 2 K. Moreover, doping of Ce⁴⁺ and Zn²⁺ at Fe³⁺ site also brings similar effects which strengthens with decreasing temperature.

Received 20th March 2018

Accepted 21st May 2018

DOI: 10.1039/c8ra02455c

rsc.li/rsc-advances

1. Introduction

Hexaferrites are widely used in electronic industries as microwave absorbers, permanent magnets, magnetic recording, data storage, *etc.* owing to their notable dielectric and magnetic properties.^{1–3} Due to low price, outstanding chemical stability and easy synthesis,⁴ M-type hexaferrites are the most extensively investigated among the common six types of hexaferrites.⁴ Recently, BaFe₁₂O₁₉ (BFO), an M-type hexaferrite, has attracted the attention of scientific community because of its tunable coercive field (H_c), reasonably high saturation magnetization (M_s), high Curie temperature (T_c), low eddy current losses and high electrical resistivity.^{5–7} By the means of suitable cationic substitutions at Ba²⁺ and/or Fe³⁺ site, saturation magnetization and coercivity of BFO can be tailor-made as per the requirements. However, while deciding outcomes of substitutions, the crystal structure of hexaferrites plays a vital role. The unit cell of BaFe₁₂O₁₉ is arranged by stacking R (BaFe₆O₁₁) and S (Fe₆O₈) blocks in RSR*S* sequence where ‘*’ denotes rotation of block along *c*-direction of the hexagonal unit cell by 180°. The R block is comprised of three hexagonal layers of oxygen with one oxygen ion in the middle layer substituted by Ba ion, while S block has two hexagonal layers with four oxygen ions in each. Five different interstitial sites are occupied by Fe³⁺ ions out of which octahedral 2a and tetrahedral 4f₁ sites are in the S block, bipyramidal 2b and octahedral 4f₂ are in R block, and octahedral 12k site resides at R–S interface. In these interstitial sites,

metal ions residing in 2a, 2b and 12k sites have spin up while in 4f₁ and 4f₂ have spin down. Total 12 Fe³⁺ ions in the formula unit are distributed on various interstitial sites as 6 ions at 12k, 2 ions at 4f₁ and 4f₂ each and 1 ion at 2a and 2b each.⁹ Since, 8 of the Fe³⁺ ions are arranged such that their spins are in the upward direction while those of remaining 4 Fe³⁺ ions are in the downward direction. Therefore, the observed net magnetic moment per formula unit is due to 4 Fe³⁺ ions in upward direction. Considering the electronic configuration of Fe³⁺, it has 5 unpaired electrons in 3d orbitals. Thus, each Fe³⁺ ion has net magnetic moment of 5 μ_B . Hence, barium hexaferrite has net magnetic moment of 20 μ_B per formula unit.

During the recent past decades, few investigations were reported on the effect doping and co-doping of various metal ions at Ba²⁺ and Fe³⁺ sites. Single substitution of metal ions such as La,⁹ Al,¹⁰ Bi,¹¹ Ti,¹² Sc,¹³ Ce,¹⁴ *etc.* and different cationic combinations such as Co–Ti,¹⁵ Bi–Ti,¹⁵ Ru–Ti,¹⁶ Zn–Sn,¹⁷ Sc–Mg,¹⁸ Zn–Ti,¹⁹ Co–Sn,²⁰ *etc.* as co-dopants at Fe³⁺ site in BaFe₁₂O₁₉ were investigated for their magnetic properties. It was observed that if Fe³⁺ ion is replaced by some non-magnetic ion, such as Zn²⁺, the saturation magnetization (M_s) is increased due to the preferred filling of tetrahedral sites by Zn²⁺ ions. Since Zn²⁺ has no net magnetic moment, therefore, it reduces the net magnetic moment in the opposite direction, eventually rendering enhanced net magnetic moment or saturation magnetization per unit formula.³ On the other hand, if magnetic cation is substituted at Fe³⁺ site, the net magnetic moment will be affected by magnetic response of dopant cation. For example, the effect of doping of Co²⁺, a magnetic cation with 3 μ_B net magnetic moment on Fe³⁺ site was studied and observed that

Department of Ceramic Engineering, Indian Institute of Technology (BHU), Varanasi, UP 221005, India. E-mail: khagesh.ktanwar.cer11@itbhu.ac.in; Tel: +91-8960482013



the net magnetization is decreased as well as the coercive field. Due to one less charge on Co^{2+} as compared to Fe^{3+} , the strength of crystal field and magnetic interaction among magnetic ions decreases leading to low coercive field.²¹ A few researchers reported the effect of Ce^{3+} doping at both Ba^{2+} and Fe^{3+} sites in $\text{BaFe}_{12}\text{O}_{19}$.^{14,22} They observed that on doping Ce^{3+} ion at Ba^{2+} site, saturation magnetization increases first and then decreases after a certain concentration (10% Ce^{3+}). However, no definite trend was observed for coercive field.¹⁴ In contrast, on doping of Ce^{3+} at Fe^{3+} site decreases the saturation magnetization because of less magnetic moment of Ce^{3+} ion as compared to Fe^{3+} . The coercive field was found to increase slightly with increasing Ce^{3+} concentration.²² Albeit, there is an uncertainty of the oxidation state of cerium as +3 and site preference of Ce^{3+} ion between Ba^{2+} and Fe^{3+} sites based on the ionic radii of these ions. All the above-mentioned reports are mainly concerned with the high temperature magnetic behavior of these hexaferrites. Therefore, it is considered worthwhile to study the magnetic behavior in low temperature region since this will strengthen the understanding of the magnetic aspects of these hexaferrites.

In the present investigation, Zn-Ce co-doped barium hexaferrites, $\text{BaFe}_{12-2x}\text{Ce}_x\text{Zn}_x\text{O}_{19}$ with $x = 0, 0.1$ and 0.3 have been synthesized *via* citrate-nitrate auto-combustion route. The magnetic behavior of synthesized hexaferrites has been investigated in low temperature regime (2–300 K). The magnetic properties are further explained by superexchange interactions and formation of Bloch walls due to imperfections.

2. Experimental work

2.1 Sample preparation

$\text{BaFe}_{12-2x}\text{Ce}_x\text{Zn}_x\text{O}_{19}$ ($x = 0.0, 0.1, 0.3$) nano-crystalline powders were synthesized using citrate nitrate auto-combustion route. Synthesized compositions were designated as BFO ($x = 0$), BFCZO1 ($x = 0.1$) and BFCZO3 ($x = 0.3$). Barium carbonate (99% purity, Sigma Aldrich), ammonium ceric nitrate (99% purity, Qualikems, India), $\text{Fe}(\text{NO}_3)_3 \cdot 9\text{H}_2\text{O}$ (98% purity, Fisher Scientific), $\text{Zn}(\text{NO}_3)_2 \cdot 9\text{H}_2\text{O}$ (96% purity, Fisher Scientific) and citric acid (99.5% purity, Loba Chemie, India) were used as the starting materials. Stoichiometric amount of BaCO_3 was weighed and dissolved in dilute nitric acid (1 : 4) to obtain $\text{Ba}(\text{NO}_3)_2$ followed by heating at 413 K till complete dryness. Ceric ammonium nitrate, barium nitrate, zinc nitrate, ferric nitrate and citric acid were then dissolved in double distilled water separately to make an aqueous transparent solution. All the prepared aqueous nitrate solutions were then added to the citric acid solution keeping the citrate to nitrate molar ratio (C/N) ~ 0.3 for controlled and smooth combustion.²³ The final mixed solution was then heated continuously at 473 K with continuous slow stirring. During heating, all the excess water evaporated, and the mass became viscous and turned into a gel. The gel slowly foamed followed by ignition and burnt into ash within a very short time-period. The ash was then collected and grounded using agate mortar-pestle. The ground powder was then calcined at 1373 K for 4 h in air. The calcined powders were then mixed with 2% PVA and pressed uniaxially under a load of

50 kN to form cylindrical pellets of diameter ~ 12 mm and thickness ~ 1.5 mm. The pellets were sintered in five steps using an electrical furnace (Lenton, made in UK). In the first step, the temperature was raised to 773 K with a heating rate of 2 K min^{-1} and held at this temperature for 1 h to remove the binder. The temperature was then raised to 1573 K (heating rate 5 K min^{-1}) and held there for 6 h and finally cooled down to the room temperature.

2.2 Characterization

HR-Powder X-ray diffraction patterns of calcined and sintered samples were recorded using Rigaku High-Resolution X-ray Diffractometer to confirm the phase purity. Data were collected in the diffraction angle (2θ) range 20 – 90° with a very slow scan rate. Rietveld refinement was carried out on HR-XRD data to determine the lattice parameters and crystal structure. In order to study the microstructure, polishing of sintered pellets was done using emery papers of grade 1/0, 2/0, 3/0, and 4/0 (Sia, Switzerland) followed by polishing on a velvet cloth using diamond paste of grade 1/4-OS-475 (HIFIN). The pellets were then thermally etched at 1473 K for 15 min, and micrographs were recorded using FEI NOVA NANOSEM 450. To study the magnetic behavior of these hexaferrite samples, the pellets were cut into cuboidal pieces of dimension $4 \text{ mm} \times 2 \text{ mm} \times 2 \text{ mm}$. M - T plots were recorded in the temperature range 2–300 K under both ZFC (zero field cooled) and FC (field cooled) conditions. M - H loops for all the samples were recorded at 2 K and 300 K while varying external magnetic field from -2 to 2 Tesla. Magnetic studies were performed using VSM (Quantum design, Model-MPMS 3, EM-QM, USA).

3. Results and discussion

3.1 Structural analysis

To confirm the phase purity of synthesized hexaferrites, HR-XRD was carried out on sintered samples in 2θ range, 20 – 100° . Fig. 1 shows the high-resolution X-ray diffraction patterns for BFO, BFCZO1 and BFCZO3. Both BFO and BFCZO1 were found to be a single phase solid solution. In BFCZO3, there were some extra peaks identified due to ceria (CeO_2). However, there were no peaks observed corresponding to ZnO or any other Zn based compounds in all the compositions. This implies that the solubility limit of cerium in hexaferrite was reached in the composition BFCZO3 while Zn was still soluble. HR-XRD data were analyzed by using X'Pert Highscore to find out initial unit cell parameters and space group. All the peaks in BFO and BFCZO1 were indexed based on JCPDS card number 78-0132. The crystal structure of BFO was found to be hexagonal with $P6_3/mmc$ space group.

To further reveal the detailed structural parameters, Rietveld refinement was carried out on HR-XRD data of all the compositions using FullProf software.²⁴ In the composition, BFCZO3 extra peaks corresponding to ceria (CeO_2) were excluded during Rietveld refinement of its HR-XRD data. During the refinement, zero correction, scale factor, lattice parameters, line widths, asymmetry parameters, atomic positions and thermal



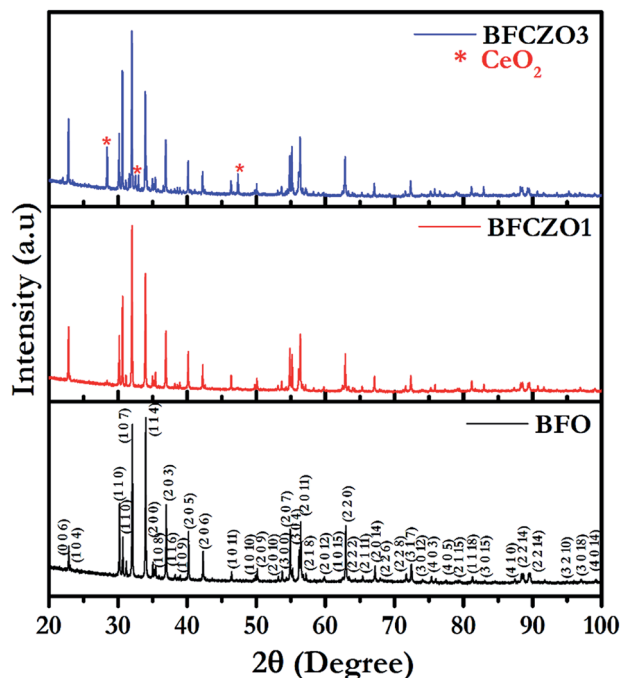


Fig. 1 High-resolution X-ray diffraction patterns for BFO, BFCZO1 and BFCZO3.

parameters were refined simultaneously. The shape of peaks was described by pseudo-Voigt function and background was expressed by linear interpolation between a set of selected background points. The fitting was judged by the goodness of fit along with low values of reliable factors such as weighted profile factor (R_{wp}), expected weighted profile factor (R_{exp}), Bragg factor (R_B) and χ^2 as included in Table 1. All the refinements were found to be a good match with experimentally observed data. Fig. 2(a) and (b) shows the Rietveld refinement fitted patterns of BFO and BFCZO1 respectively. All the important refined parameters are given in Tables 1 and 2 and bond lengths and bond angles are reported in Tables 3 and 4 respectively. Bond lengths and bond angles for the composition, BFCZO3 are not included due to presence of ceria as an extra phase in this composition. Lattice parameters of BFO closely match with the previously reported data.²⁵ With increasing doping concentration of Ce^{4+} and Zn^{2+} at the Fe^{3+} site, the lattice parameters were found to be increased. The lattice parameter ' c ' was increased

Table 1 Cell parameters and other reliable parameters of Rietveld analysis for BFO, BFCZO1 and BFCZO3

Parameters	BFO	BFCZO1	BFCZO3
a (Å)	5.8908	5.8959	5.8993
b (Å)	5.8908	5.8959	5.8993
c (Å)	23.2075	23.2259	23.2422
R_p	30.7	38.4	49.4
R_{wp}	17.3	25.2	31.8
R_{exp}	15.4	14.6	16.3
R_B	6.87	13.47	14.3
χ^2	1.26	2.98	3.78

more as compared to ' a or b ' which is due to presence of multiple Fe^{3+} sites along c -axis as compared to a and b -axis. It is interesting to note from Table 2 that B_{iso} for Fe^{3+} at trigonal bipyramidal (TBP) is high as compared to that in octahedral and tetrahedral sites. In addition, the Fe–O average bond length in TBP site is significantly high as compared to average bond length in octahedral and tetrahedral sites. This indicates that Fe^{3+} at TBP site has high dynamics due to thermal energy. Furthermore, the bond angles (see Table 4) also deviates from standard bond angles in octahedra, tetrahedra and TBP sites. The existence of large bond lengths, high dynamics of Fe^{3+} at TBP site due to thermal energy coupled with significant deviation of bond angles from standard values would affect the magnetic exchange interaction in these ferrites which is discussed in detail in Section 3.3.

3.2 Site preference of Ce^{4+} and Zn^{2+}

It has been reported in previous studies that Zn^{2+} prefers $4f_1$ site among all the available Fe^{3+} sites.³ However, there is an uncertainty with site preference of Ce. A few studies suggested that the Ce preferably occupy Ba-site,¹⁴ meanwhile, other reports claimed that Ce prefers Fe-site.²² In the present study, we have assumed that Ce would occupy the Fe-site and hence synthesized compounds accordingly. Considering the ionic radius of Ce^{4+} (0.87 Å)²⁶ and Ba^{2+} (1.61 Å),²⁶ it is clear that if Ce^{4+} replaces Ba^{2+} , then final lattice parameters should decrease. But, in the current study, lattice parameters were found to increase with increasing Ce^{4+} concentration. Moreover, the ionic radius of Ce^{4+} (0.87 Å)²⁶ is much closer to Fe^{3+} (0.78 Å)²⁶ as compared to Ba^{2+} (1.61 Å).²⁶ Thus Ce^{4+} would prefer Fe^{3+} site instead of Ba^{2+} site. For further investigations, HR-XRD of BFO and BFCZO1 was compared. Interestingly, the intensities of a few reflections such as (006), (008) and (107) were increased substantially as depicted in Fig. 3 while rest of the pattern remained unaltered. The schematic of BFO with (006), (008) and (107) planes is shown in Fig. 3. It is observed from the Fig. 3 that these planes contain only Fe sites. Therefore, the intensities of HR-XRD profiles will differ only in these directions. Hence, it can be concluded that Ce^{4+} ions occupy Fe^{3+} sites instead of Ba^{2+} .

3.3 Microstructural analysis

Microstructure plays a key role in defining magnetic properties of hexaferrites.^{27–29} In hexaferrites c -axis is easy axis of magnetization.³⁰ If the grain growth occurs favorably along c -direction, then it will affect the coercive field of the material.³¹ This eventually can change the behavior of the sample from hard magnetic to a typical soft magnetic. In addition, the grain size also can affect the magnetic behavior.²⁷ For example, in case of smaller grains there would be high pinning of magnetic moments at the grain boundaries resulting into high coercive field.³² In contrast, a single crystal or a single grain would have almost negligible coercive field if studied while applying external field along c -axis (easy axis). This type of behavior was reported in previous studies.³²

The microstructure of these hexaferrites was studied using HR-SEM. Images of fractured surface of BFO, BFCZO1 and



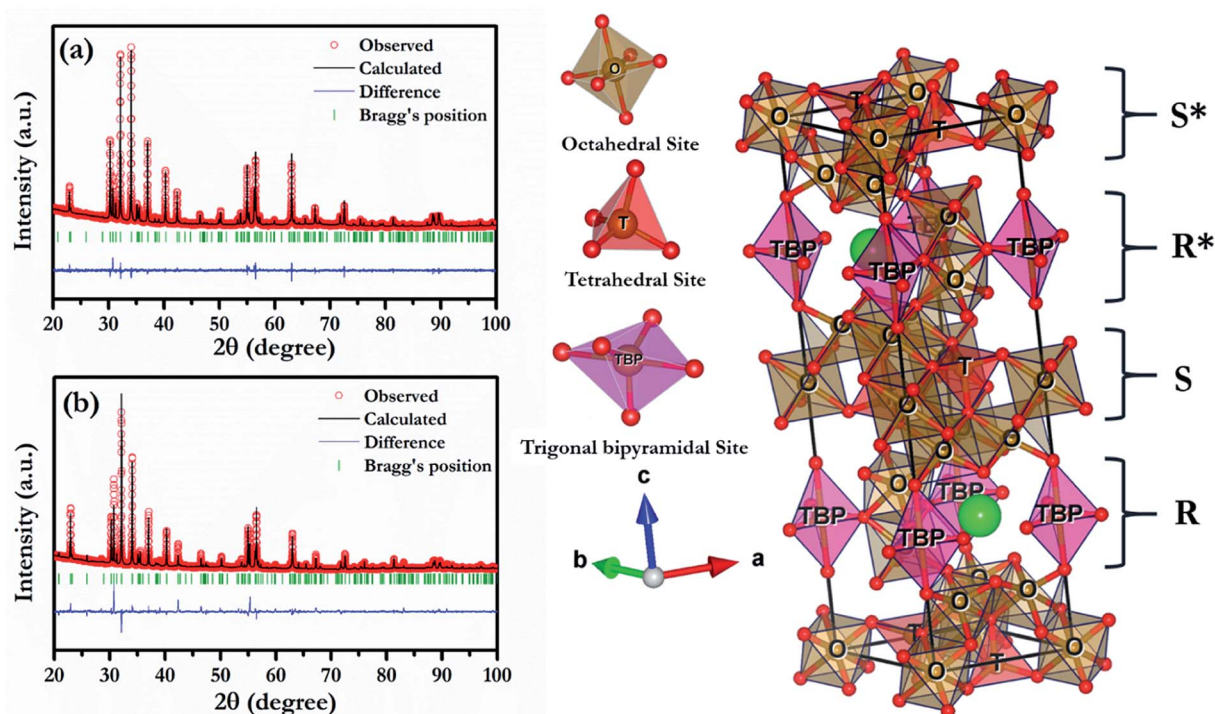


Fig. 2 Rietveld refinement patterns of (a) BFO, (b) BFCZO1 and schematic of BFO.

BFCZO3 are depicted in Fig. 4a, c and d respectively. Grains with plate-like shape having high aspect ratio appears to grow along the *c*-axis. It is interesting to note that the aspect ratio of grains in BFO is very large which decreases substantially on substitution of Zn^{2+} and Ce^{4+} . In the composition, BFCZO3, large hexagonal shaped grains were observed. However, the average grain size increases with increasing dopant concentrations. The average grain size was measured assuming grains of spherical shape. The average grain size of BFO, BFCZO1 and BFCZO3 was found to be 0.61 μm , 1.32 μm and 2.49 μm respectively. It can be inferred by comparing the grain size that doping of Ce^{4+} and Zn^{2+} suppresses grain growth specially along *c*-axis. It is noted that addition of Ce^{4+} and Zn^{2+} favors the formation of grains

with high volume. These large hexagonal grains may be consisting of multi-domains.³³ The effect of multi-domain grains on magnetization of these hexagonal ferrites is further discussed in Section 3.4. Fig. 4(b) shows the EDX elemental mapping of BFO sample. It was inferred from the compositional analysis that the stoichiometry of different atoms was well maintained as per requirement in M-type hexaferrites.

3.4 Magnetic properties

Variation of Magnetization with temperature, in the temperature range 2–300 K, for both FC (cooling and heating in the presence of 300 Oe external magnetic field) and ZFC (cooling in

Table 2 Refined structural parameters of Rietveld analysis for BFO and BFCZO1

Atoms	BaFe ₁₂ O ₁₉ (BFO)				BaCe _{0.1} Zn _{0.1} Fe _{11.8} O ₁₉ (BFCZO1)			
	X	Y	Z	<i>B</i> _{iso}	X	Y	Z	<i>B</i> _{iso}
Ba	0.6667	0.3333	0.2500	0.78	0.6667	0.3333	0.2500	0.31
Fe1	0.0000	0.0000	0.0000	0.90	0.0000	0.0000	0.0000	0.56
Fe2	0.0000	0.0000	0.2500	2.17	0.0000	0.0000	0.2500	3.68
Fe3	0.3333	0.6667	0.0282	0.59	0.3333	0.6667	0.0281	0.24
Zn	—	—	—	—	0.3333	0.6667	0.0281	0.23
Fe4	0.3333	0.6667	0.1908	0.69	0.3333	0.6667	0.1940	1.06
Ce	—	—	—	—	0.3333	0.6667	0.1940	1.06
Fe5	0.1681	0.3374	−0.1086	0.59	0.1684	0.3369	−0.1098	0.22
O1	0.0000	0.0000	0.1480	0.58	0.0000	0.0000	0.1253	2.28
O2	0.3333	0.6667	−0.0565	0.89	0.3333	0.6667	−0.0868	1.18
O3	0.1802	0.3605	0.2500	0.32	0.1970	0.3942	0.2500	1.67
O4	0.1629	0.3257	0.0517	0.15	0.1777	0.3553	0.0469	0.34
O5	0.5033	0.0068	0.1467	0.07	0.5083	0.0167	0.1249	1.14



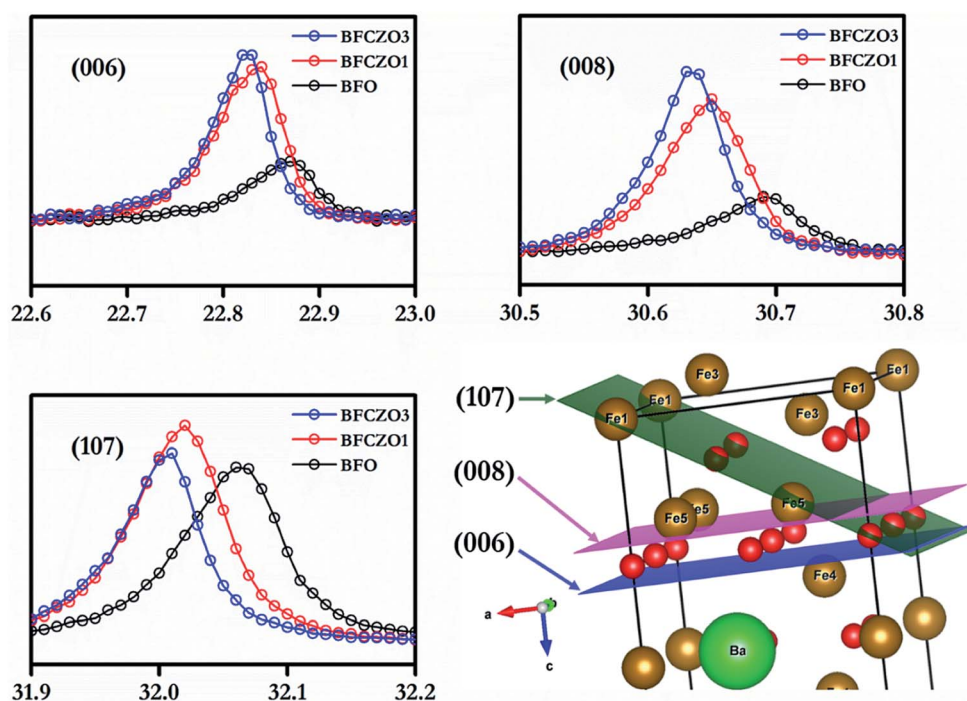
Table 3 Different Fe–O (Me–O) and average bond lengths for BFO and BFCZO1; O–octahedral, TBP–trigonal bipyramidal, T–tetrahedral

Site	Bond type	Bond length (Å)		Average bond length (Å)	
		BFO	BFCZO1	BFO	BFCZO1
Fe1 (2a, O)	Fe1–O4	2.04994	2.11640	2.04994	2.11640
Fe2 (2b, TBP)	Fe2–O1	2.36694	2.89557	2.05031	2.37576
	Fe2–O3	1.83923	2.01255		
Fe3 (4f ₁ , T)	Fe3–O2	1.96591	2.66889	1.85881	1.90412
	Fe3–O4	1.82311	1.64920		
Fe4 (4f ₂ , O)	Fe4–O3	2.08050	1.90391	2.04747	2.15324
	Fe4–O5	2.01444	2.40258		
Fe5 (12k, O)	Fe5–O1	1.94911	1.75753	2.01572	1.91466
	Fe5–O2	2.06924	1.76621		
	Fe5–O4	2.14641	2.29335		
	Fe5–O5	1.89156	1.68877		

Table 4 Me₁–O–Me₂ (Me=Fe) bond angles for BFO and BFCZO1

Bond type	BFO	BFCZO1
Fe1–O4–Fe3	126.7153	133.5897
Fe1–O4–Fe5	93.3023; 93.3011	88.3533; 88.3464
Fe2–O1–Fe5	117.9775	101.8584
Fe2–O3–Fe4	138.6468	136.9580
Fe3–O2–Fe5	125.7317	107.5496
Fe4–O3–Fe4	82.7063	86.0841
Fe4–O5–Fe5	127.8448; 127.8131	118.7285; 118.7063
Fe5–O2–Fe5	89.3373	111.3225
Fe5–O5–Fe5	100.5177	119.4773

absence of magnetic field and heating in presence of 300 Oe external magnetic field) conditions is depicted in Fig. 5. All the synthesized compositions exhibited an increasing trend of magnetization in both ZFC and FC conditions. The net magnetization in FC condition was higher than that in ZFC because the sample was cooled in presence of 300 Oe external field during FC. The net magnetization increased with decreasing temperature. This increase in magnetization is due to the stability of magnetic moments and strong coupling between magnetic dipoles at low temperature.³⁴ At 300 K, the net magnetization doesn't become zero which shows that the Curie temperature lies beyond this temperature range. The Curie temperature in these hexaferrites was reported to be around 500 K.³⁵ Interestingly, the net magnetic moment increases with doping of Ce⁴⁺ and Zn²⁺. As stated earlier, Zn²⁺, a non-magnetic ion, prefers 4f₁ site. Since, 4f₁ site carries the magnetic moment in opposite direction to net magnetic moment of the unit cell, therefore replacing Fe³⁺ by a non-magnetic ion, Zn²⁺, on this particular site would eventually enhance the net magnetization.³ On the other hand, Ce⁴⁺ replaces one of the Fe³⁺ ions at three octahedra sites, 12k, 4f₂ and 2a. Thus, the effect of Ce⁴⁺ on net magnetization is rather difficult to predict. However, to gain impetus into the effect of Ce⁴⁺ doping on net magnetization, it is important to compare the magnetic behavior of BFCZO1 and BFCZO3. From the Fig. 5, it is noticed that increase in net magnetization of BFCZO1 as compared to BFO is ~3 emu/gm while in BFCZO3 its ~1.6 emu gm^{−1} with respect to BFCZO1. Thus, in BFCZO1, the increase in net magnetization is due to combined effect of Ce⁴⁺ and Zn²⁺. Whereas, further increased magnetization in BFCZO3 seems to be due to the occupation of 4f₁ site by Zn²⁺ and partial occupation of Ce⁴⁺ on 4f₂ site, since in this composition Ce⁴⁺ is not

**Fig. 3** Comparison of (006), (008) and (107) HR-XRD profiles and intersections of these planes in unit cell.

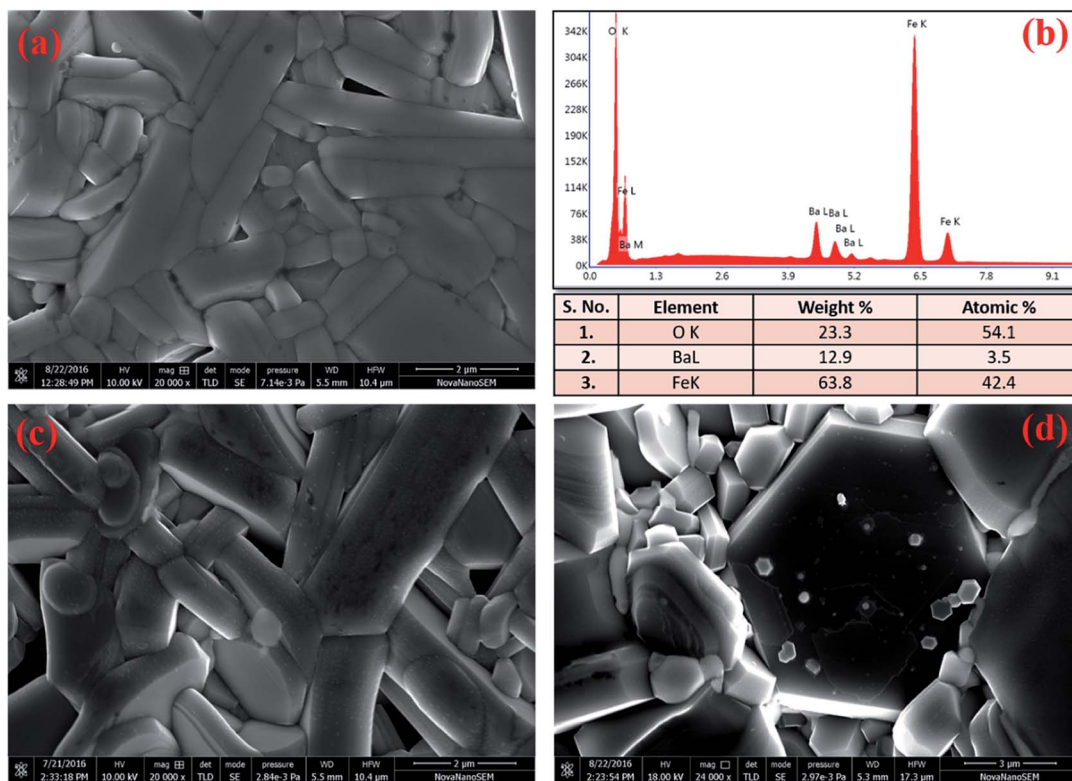


Fig. 4 HR-SEM images of (a) BFO, (c) BFCZO1, (d) BFCZO3 and (b) EDX elemental mapping results for BFO.

fully blended in solid solution as observed in HR-XRD. Therefore, it can be expected that Ce^{4+} preferably favors $4f_2$ site. However, exact site occupation of Ce^{4+} is still uncertain.

Fig. 6(a) and 7(a) show the M - H hysteresis loop of BFO, BFCZO1 and BFCZO3 at 300 K and 2 K respectively, in the range of -2 to $+2$ Tesla. All the compositions were saturated in this range of external magnetic field. The values of saturation magnetization (M_s), remanent magnetization (M_R) and coercive field (H_C) are given in Table 5. The saturation magnetization (M_s) was calculated using Law of approach to saturation (LAS)³⁶ described by eqn (1).

$$M = M_s \left(1 - \frac{A}{H} - \frac{B}{H^2} \right) + \chi_p H \quad (1)$$

where, M_s is saturation magnetization, 'A' is inhomogeneity parameter, χ_p is the high field susceptibility and 'B' is anisotropy parameter. For hexagonal ferrites, 'B' can be expressed by eqn (2):³⁶

$$B = \frac{8K_1^2}{105M_s^2} \quad (2)$$

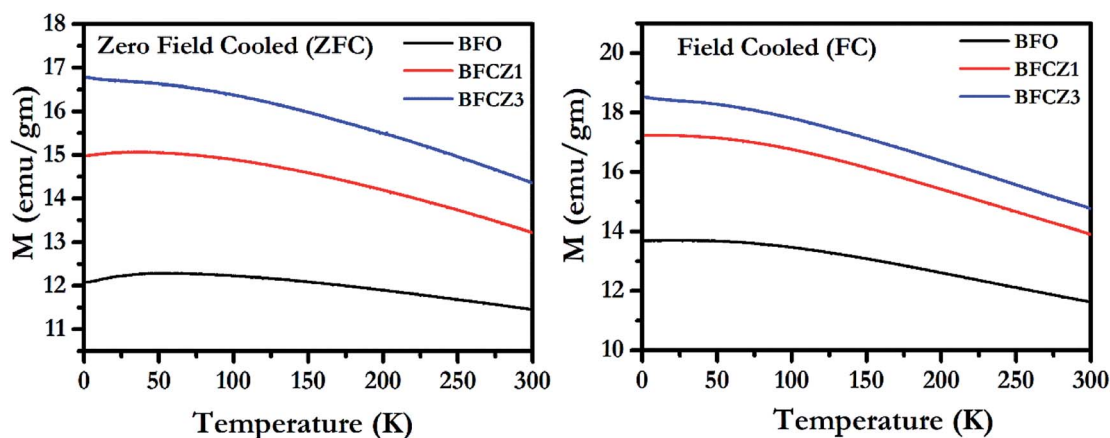


Fig. 5 Magnetization vs. temperature plot for BFO, BFCZO1 and BFCZO3 in both ZFC and FC conditions.



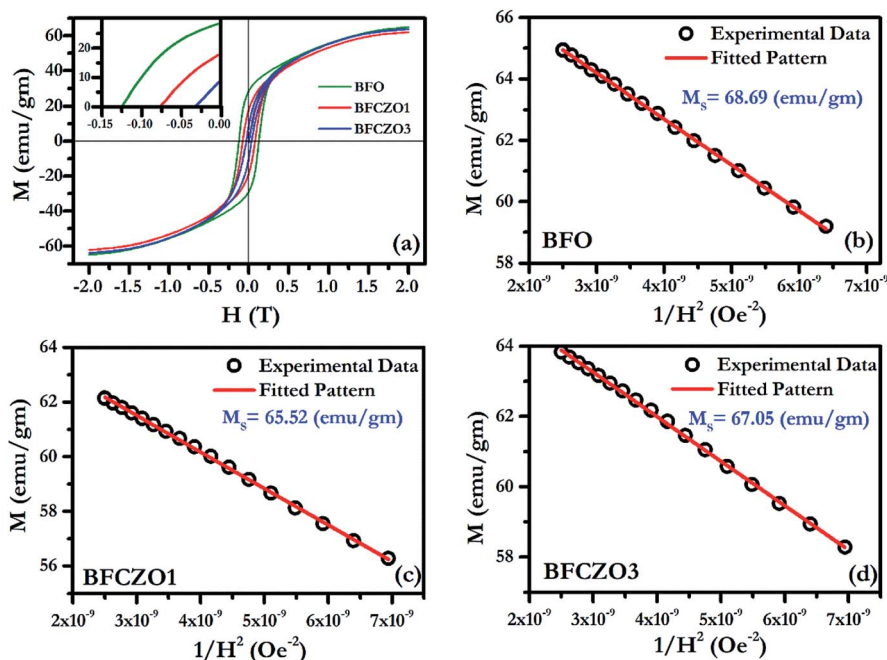


Fig. 6 (a) $M-H$ hysteresis loop for BFO, BFCZO1 and BFCZO3 at 300 K, (b), (c) and (d) Fitting of $M-H$ data in high field regime for BFO, BFCZO1 and BFCZO3 respectively.

Moreover, at the sufficiently high magnetic field the value of A/H and χ_P in eqn (1) are negligible in case of hexaferrites as explained by Neel³⁷ and Brown.³⁸ Thus, the eqn (1) can be written as follows:

$$M = M_s \left(1 - \frac{8K_1^2}{105M_s^2 H^2} \right) \quad (3)$$

To calculate the saturation magnetization (M_s) and K_1 , $M-H$ curve data at high external field were fitted with the eqn (3). The fitted curves, according to the equation above, for all the compositions at 300 K and 2 K are depicted in Fig. 6(b-d) and 7(b-d) respectively. On the basis of M_s and K_1 , the values of the anisotropy field (H_a) can be calculated by the eqn (4):^{33,39}

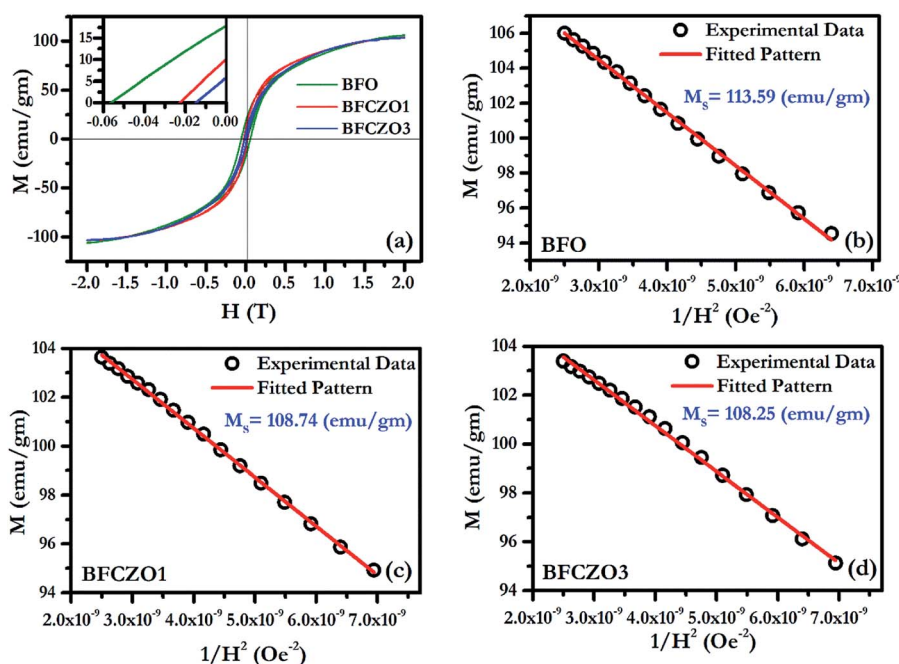


Fig. 7 (a) $M-H$ hysteresis loop for BFO, BFCZO1 and BFCZO3 at 2 K, (b), (c) & (d) Fitting of $M-H$ data in high field regime for BFO, BFCZO1 and BFCZO3 respectively.



Table 5 Saturation magnetization, coercive field, remanent magnetization, M_R/M_S ratio, anisotropy field (H_A) and magnetocrystalline anisotropy constant (K_1) for all the compositions at 300 K and 2 K

Compositions/ properties	300 K			2 K		
	BFO	BFCZO1	BFCZO3	BFO	BFCZO1	BFCZO3
M_S (emu gm ⁻¹)	68.69	65.52	67.05	124.91	117.28	117.44
H_C (Oe)	1238	752	306	558	227	146
M_R (emu gm ⁻¹)	28	18	7	18	10	6
M_R/M_S	0.41	0.27	0.10	0.14	0.08	0.05
H_A ($\times 10^4$)	7.24	7.02	6.81	8.01	6.68	6.52
K_1 ($\times 10^6$)	2.49	2.30	2.28	4.55	3.63	3.53

$$H_a = \frac{2K_1}{M_s} \quad (4)$$

where, H_A is anisotropy field, M_S is saturation magnetization and K_1 is magneto-crystalline anisotropy (MCA) constant. The values of K_1 and H_A are listed in Table 5. The degree of MCA is defined by H_A , in A m⁻¹, and anisotropy constant K_1 is a measure of the difficulty to move the magnetization out of preferred (easy) direction in the crystal lattice.^{4,40} MCA is related to the energy needed to turn a magnetization vector from the preferred low energy, or easy direction, to a difficult, higher energy orientation, represented by the anisotropy constants K_1 and K_2 . For single hexagonal crystals the total anisotropy energy (E_A) is given by the sum:⁴¹

$$E_A = \sum_K K_0 + K_1 \sin^2 \varphi + K_2 \sin^4 \varphi + \dots \quad (5)$$

where K_0 = the energy to magnetize along the easy axis, and φ = the angle between the direction of magnetization and the c -axis. The higher order terms (K_2 , K_3 ...) are negligible for uniaxial ferrites.⁴² K_0 has a low value as the easy axis is a low energy orientation.⁴ Thus, for M-type hexaferrites the anisotropy constant becomes K_1 .

At 300 K, maximum saturation magnetization, 68.69 emu gm⁻¹ was found in BFO. Interestingly, doping of Ce⁴⁺ and Zn²⁺ in BFO reduces M_R and H_C substantially while M_S remains almost invariant as shown in Table 5. The effect of Ce⁴⁺ and Zn²⁺ on magnetic behavior of these samples can be explained on the basis of the presence of large grains with low aspect ratio. These large grains can be considered as comprised of multiples crystallites. Kittel⁴³ suggested that if the crystallite size surpasses a critical diameter, Bloch walls will be created spontaneously.³² Due to presence of these multiple crystallites, there will be randomly oriented multiple domains with a net magnetization in a single grain. Thus, at 300 K, after doping with Ce⁴⁺ and Zn²⁺, presence of excessive additional domains would help to decrease the remanent magnetization and coercive field. However, it was observed by Rathenau *et al.*³² that the formation of Bloch walls is not constrained to particle size; rather it depends upon the presence of imperfections. In the present case, due to introduction of Ce and Zn, presence of defects such as oxygen vacancies can be expected. Presence of these vacancies (imperfections) would enhance Bloch wall

formation around the imperfections and hence result in the reduced remanent magnetization and coercive field. To further verify this, we have calculated M_R/M_S ratio, anisotropy constant K_1 and highest coercive force (H_A) (see Table 5). It has been observed that the M_R/M_S ratio is 0.40 for BFO which is closer to 0.50, values for well oriented samples.⁴² In case of BFCZO1 and BFCZO3, it reduced to 0.27 and 0.10 respectively. These low values of M_R/M_S imply the enhanced disorientated domains and hence low M_R and H_C . From the Table 5, it can be observed that M_R reduced by ~35% and ~75% in BFCZO1 and BFCZO3 respectively as compared to BFO. H_C decreased by ~40% and ~76% in BFCZO1 and BFCZO3 respectively.

The scenario at low temperature (2 K) is quite similar to 300 K. At 2 K, the saturation magnetization becomes almost double in all the compositions. The remanent magnetization and coercive field also follow similar trend with increasing Ce⁴⁺ and Zn²⁺ concentrations. But, the remanent magnetization and coercive field in BFO decrease manifold at low temperature. To understand this behavior, one has to consider exchange interactions in these hexaferrites.⁴⁴ Generally, in metals, the magnetic spins are linked to each other *via* direct exchange which becomes negligible over longer distances. In these ferri-magnets, the distance between two magnetic ions is not adequate, due to presence of oxygen ions, for direct exchange. Thus, magnetic moments are linked by superexchange interactions. The interaction of opposing magnetic spins *via* an intermediate oxygen atom (Me₁-O-Me₂) (Me-magnetic ion and O-oxygen) is known as superexchange interaction.⁴⁵ The magnitude of superexchange interaction can be estimated by Me₁-O-Me₂ bond angles and bond lengths. An angle of 180° (Me₁-O-Me₂) would cause strongest interaction effect and 90° weakest, and the effect becomes negligible over Me-O distance of 3 Å, as suggested by Anderson.⁴⁶ In the present case, to evaluate the effect of superexchange interaction we have calculated all the possible Me-O bond lengths and Me-O-Me bond angles, as listed in Tables 3 and 4. All the bond lengths in BFO and BFCZO1 are less than 3 Å. Therefore, superexchange interactions are significant at all the Fe³⁺ sites. The average bond length follows TBP > O > T order at 300 K. Thus, tetrahedra Fe³⁺ sites have strongest interaction while TBP sites have the weakest interaction. Furthermore, as observed in HR-XRD, the thermal parameter is also high for Fe³⁺ ions at TBP site. This leads to weak exchange interaction and hence less contribution in net magnetization at 300 K. At 2 K, it is expected that all the sites are frozen and superexchange interactions are enhanced. However, as observed from Tables 3 and 4, the Me-O-Me bond angles around 4f₁ and 4f₂ site are rather closer to 180° thus the interaction would be strong in these sites as compared to the other sites. Hence, at low temperature, it can be hypothesized that when external magnetic field is applied, all the magnetic moments are being forced to align in the direction of external field. As the external field is reduced slowly, due to strong interactions of magnetic moments in opposite directions (4f₁ and 4f₂ sites), they tend to return to their original position. In this way, they also force to relax the magnetic moments which are in the direction of net magnetization resulting in low remanent magnetization and coercive force. To further verify



the hypothesis, we have calculated the M_R/M_S ratio, anisotropy constant K_1 and anisotropy field H_A at 300 K and 2 K. Interestingly, M_R/M_S ratio decreases from 0.41 to 0.14 while the values of K_1 and H_A increased substantially as compared to the values obtained at 300 K in BFO. As a whole, all these values will decrease remanent magnetization and coercive force as discussed above. However, a decreasing trend of K_1 and H_A , an anomalous behavior, was observed with doping of Ce^{4+} and Zn^{2+} in BFO. In doped compositions, BFCZO1 and BFCZO3, due to presence of non-magnetic ions, the superexchange interaction would be weakened. Hence, the anisotropy constant K_1 and highest coercive force H_A would also decrease, as observed from Table 5. The effect doping Ce^{4+} and Zn^{2+} collectively, changes its behavior from hard to soft magnet.

4. Conclusions

In summary, $BaFe_{12-2x}Ce_xZn_xO_{19}$ ($x = 0.0, 0.1, 0.3$) samples were successfully synthesized *via* citrate-nitrate auto-combustion route and conventional sintering at 1573 K. High-resolution X-ray diffraction and scanning electron microscopy studies were carried out to reveal the phase purity and morphology. Rietveld refinement of HR-XRD data was done to divulge the structural parameters such as lattice parameters, bond angles, bond lengths, thermal parameters and atomic positions. Magnetic behavior all the samples were studied in low temperature regime, 2–300 K. With decreasing temperature, all the samples convert their behavior from hard to soft magnet. The doping of Ce^{4+} and Zn^{2+} in BFO suppresses the *c*-axis preferred grain growth and enhances the average grain size. The presence of these non-magnetic ions in BFO helped to decrease the remanent magnetization at 300 K and 2 K altering their behavior from hard to soft magnet. The magnetic behavior was explained on the Bloch wall formation and superexchange interactions.

Conflicts of interest

There are no conflicts of interest to declare.

References

- 1 A. Ghasemi, S. E. Shirsath, X. Liu and A. Morisako, *J. Appl. Phys.*, 2011, **109**, 07A507.
- 2 Ü. Özgür, Y. Alivov and H. Morkoç, *J. Mater. Sci. Mater. Electron.*, 2009, **20**, 789–834.
- 3 Z. W. Li, C. K. Ong, Z. Yang, F. L. Wei, X. Z. Zhou, J. H. Zhao and A. H. Morrish, *Phys. Rev. B*, 2000, **62**, 6530–6537.
- 4 R. C. Pullar, *Prog. Mater. Sci.*, 2012, **57**, 1191–1334.
- 5 W. Gong, G. C. Hadjipanayis and R. F. Krause, *J. Appl. Phys.*, 1994, **75**, 6649–6651.
- 6 P. Campbell, *Permanent Magnet Materials and their Application*, Cambridge University Press, Cambridge, 1994.
- 7 S. Castro, M. Gayoso, J. Rivas, J. M. Greneche, J. Mira and C. Rodríguez, *J. Magn. Magn. Mater.*, 1996, **152**, 61–69.
- 8 R. C. Pullar, *Prog. Mater. Sci.*, 2012, **57**, 1191–1334.
- 9 C. Wu, Z. Yu, K. Sun, J. Nie, R. Guo, H. Liu, X. Jiang and Z. Lan, *Sci. Rep.*, 2016, **6**, 36200.
- 10 V. N. Dhage, M. L. Mane, A. P. Keche, C. T. Birajdar and K. M. Jadhav, *Phys. B*, 2011, **406**, 789–793.
- 11 P. Winotai, S. Thongmee and I. M. Tangab, *Mater. Res. Bull.*, 2000, **35**, 1747–1753.
- 12 P. A. Mariño-Castellanos, J. Anglada-Rivera, A. Cruz-Fuentes and R. Lora-Serrano, *J. Magn. Magn. Mater.*, 2004, **280**, 214–220.
- 13 P. Borisov, J. Alaria, T. Yang, S. R. C. McMitchell and M. J. Rosseinsky, *Appl. Phys. Lett.*, 2013, **102**, 1–6.
- 14 Z. Mosleh, P. Kameli, A. Poorbaferani, M. Ranjbar and H. Salamati, *J. Magn. Magn. Mater.*, 2016, **397**, 101–107.
- 15 A. G. Belous, O. I. V'yunov, E. V. Pashkova, V. P. Ivanitskii and O. N. Gavrilenko, *J. Phys. Chem. B*, 2006, **110**, 26477–26481.
- 16 A. M. Alsmadi, I. Bsoul, S. H. Mahmood, G. Alnawashi, K. Prokeš, K. Siemensmeyer, B. Klemke and H. Nakotte, *J. Appl. Phys.*, 2013, **114**, 4–12.
- 17 H. C. Fang, Z. Yang, C. K. Ong, Y. Li and C. S. Wang, *J. Magn. Magn. Mater.*, 1998, **187**, 129–135.
- 18 Y. Tokunaga, Y. Kaneko, D. Okuyama, S. Ishiwata, T. Arima, S. Wakimoto, K. Kakurai, Y. Taguchi and Y. Tokura, *Phys. Rev. Lett.*, 2010, **105**, 17–20.
- 19 P. Wartewig, M. K. Krause, P. Esquinazi, S. Rösler and R. Sonntag, *J. Magn. Magn. Mater.*, 1999, **192**, 83–99.
- 20 F. Sandiumenge, B. Martínezxavier, X. Batlle, S. Gali and X. Obradors, *J. Appl. Phys.*, 1992, **72**, 4608.
- 21 M. G. Shalini and S. C. Sahoo, *AIP Conf. Proc.*, 2016, **1728**, 020445.
- 22 R. A. Pawar, S. S. Desai, Q. Y. Tamboli, S. E. Shirsath and S. M. Patange, *J. Magn. Magn. Mater.*, 2015, **378**, 59–63.
- 23 K. Tanwar, N. Jaiswal, D. Kumar and O. Parkash, *J. Alloys Compd.*, 2016, **684**, 683–690.
- 24 J. Rodrigues-Carvajal, Lab. Leon Brillouin, CEA-CNRS, Fr., 2000.
- 25 P. B. Braun, *The crystal structures of a new group of ferromagnetic compound*, 1957.
- 26 R. D. Shannon and C. T. Prewitt, *Acta Crystallogr., Sect. B: Struct. Crystallogr. Cryst. Chem.*, 1969, **25**, 925–946.
- 27 M. Hillert, *Acta Metall.*, 1965, **13**, 227–238.
- 28 J. Dho, E. K. Lee, J. Y. Park and N. H. Hur, *J. Magn. Magn. Mater.*, 2005, **285**, 164–168.
- 29 S. Ram, H. Krishnan, K. Rai and K. Narayan, *Jpn. J. Appl. Phys.*, 1989, **28**, 604–608.
- 30 X. Zhang, Z. Yue, S. Meng and L. Yuan, *J. Appl. Phys.*, 2015, **116**, 243909.
- 31 M. Sugimoto, *J. Am. Ceram. Soc.*, 1999, **82**, 269–280.
- 32 G. W. Rathenau, *Rev. Mod. Phys.*, 1953, **25**, 297–301.
- 33 C. Kittel, *Rev. Mod. Phys.*, 1949, **21**, 541–583.
- 34 H. Kojima, *Handb. Ferromagn. Mater.*, 1982, vol. 3, pp. 305–391.
- 35 L. Jahn and H. G. Muller, *Phys. Status Solidi*, 1963, **35**, 723–730.
- 36 T. Miyazaki and H. Jin, *The Physics of Ferromagnetism*, Oxford University Press, 2012, vol. 158.
- 37 L. Néel, *J. Phys. Radium*, 1948, **9**, 184–192.



- 38 W. F. Brown, *Phys. Rev.*, 1941, **60**, 139–147.
- 39 A. Moitra, S. Kim, S. G. Kim, S. C. Erwin, Y. K. Hong and J. Park, *Comput. Condens. Mat.*, 2014, **1**, 45–50.
- 40 B. T. Shirk, *J. Appl. Phys.*, 1969, **40**, 1294.
- 41 C. Heck, *Magnetic Materials and their Applications*, London: Butterworth, 1974.
- 42 J. Smit and H. P. J. Wijn, *Ferrites: physical properties of ferrimagnetic oxides in relation to their technical applications*, Philips' Technical Library, Eindhoven, Netherlands, 1959, p. 369.
- 43 C. Kittel, *Phys. Rev.*, 1948, **73**, 810–811.
- 44 L. Néel, *Proc. Phys. Soc., Sect. A*, 1952, **65**, 869–885.
- 45 H. Kramers, *Physica*, 1934, **1**, 182–192.
- 46 P. W. Anderson, *Phys. Rev.*, 1950, **79**, 705–710.

